OPEN ACCESS



Strong Mg II and Fe II Absorbers at 2.2 < z < 6.0

Siwei Zou¹, Linhua Jiang^{1,2}, Yue Shen^{3,4}, Jin Wu^{1,2}, Eduardo Bañados⁵, Xiaohui Fan⁶, Luis C. Ho^{1,2}, Dominik A. Riechers⁷, Bram Venemans⁵, Marianne Vestergaard^{6,8}, Fabian Walter⁵, Feige Wang⁶, Chris J. Willott⁹, Ravi Joshi¹, Xue-Bing Wu^{1,2}, and Jinyi Yang⁶.

Kavli Institute for Astronomy and Astrophysics, Peking University, Beijing 100871, People's Republic of China; zousiwei@pku.edu.cn, jiangKIAA@pku.edu.cn

Department of Astronomy, School of Physics, Peking University, Beijing 100871, People's Republic of China

Department of Astronomy, University of Illinois at Urbana-Champaign, Urbana, IL 61801, USA

National Center for Supercomputing Applications, University of Illinois at Urbana-Champaign, Urbana, IL 61801, USA

Max Planck Institut für Astronomie, Königstuhl 17, D-69117, Heidelberg, Germany

Steward Observatory, University of Arizona, 933 N Cherry Avenue, Tucson, AZ 85721, USA

Cornell University, Space Sciences Building, Ithaca, NY 14853, USA

Niels Bohr Institute, University of Copenhagen, Jagtvej 128, DK-2200 Copenhagen, Denmark

NRC Herzberg, 5071 West Saanich Road, Victoria, BC V9E 2E7, Canada

Received 2020 May 6; revised 2020 October 19; accepted 2020 October 28; published 2021 January 4

Abstract

We present a study of strong intervening absorption systems in the near-IR spectra of 31 luminous quasars at z > 5.7. The quasar spectra were obtained with Gemini GNIRS that provide continuous wavelength coverage from \sim 0.9 to \sim 2.5 μ m. We detect 32 strong Mg II doublet absorbers with rest-frame equivalent width $W_r(\lambda 2796) > 1.0$ Å at 2.2 < z < 6.0. Each Mg II absorber is confirmed by at least two associated Fe II absorption lines in the rest-frame wavelength range of \sim 1600–2600 Å. We find that the comoving line density (dN/dX) of the strong Fe II-bearing Mg II absorbers decreases toward higher redshift at z > 3, consistent with previous studies. Compared with strong Mg II absorbers detected in damped Ly α systems at 2 < z < 4, our absorbers are potentially less saturated and show much larger rest-frame velocity widths. This suggests that the gas traced by our absorbers are potentially affected by galactic superwinds. We analyze the Hubble Space Telescope near-IR images of the quasars and identify possible associated galaxies for our strong absorbers. There are a maximum of two galaxy candidates found within 5" radius of each absorber. The median F105W-band magnitude of these galaxy candidates is 24.8 mag, which is fainter than the L^* galaxy luminosity at $z \sim 4$. By using our observed dN/dX of strong Mg II absorbers and galaxy candidates median luminosity, we suggest that at high redshift, strong Mg II absorbers tend to have a more disturbed environment but smaller halo size than that at z < 1.

Unified Astronomy Thesaurus concepts: Circumgalactic medium (1879); Extragalactic astronomy (506); Quasar absorption line spectroscopy (1317)

1. Introduction

The circumgalactic medium (CGM) is defined as the gas around the disk or interstellar medium of a galaxy typically within the virial radius of the galaxy. Previous studies suggested that the physical conditions of the gas in the CGM are influenced by both cold accretion inflows and galactic outflows (see Tumlinson et al. 2017 for a review and references therein). Studies of absorption lines toward bright background sources such as quasars provide a unique and powerful tool to study the physical conditions of the gas. Among these absorption lines, the low-ionization Mg II $\lambda\lambda$ 2796,2803 doublet is found to be associated with cool components (T $\sim 10^4$ K) in CGM (Bergeron & Boissé 1991; Steidel et al. 2002). Observationally, the connection between the Mg II absorption and CGM is studied using quasar-galaxy pairs at low redshift. By comparing the kinematics of absorbers and galaxies, Mg II has been shown to trace both metal-enriched infalling gas (Chen et al. 2010; Lovegrove & Simcoe 2011; Kacprzak et al. 2011; Rubin et al. 2012; Bouché et al. 2013; Zabl et al. 2019), and outflows from luminous star-forming galaxies (Bouché et al. 2006; Martin & Bouché 2009; Noterdaeme et al. 2010;

Original content from this work may be used under the terms of the Creative Commons Attribution 4.0 licence. Any further distribution of this work must maintain attribution to the author(s) and the title of the work, journal citation and DOI.

Ménard & Fukugita 2012; Schroetter et al. 2016, 2019). Zabl et al. (2019) studied nine quasar–galaxy pairs that were selected from 79 Mg II absorbers at $z \sim 1$. They found that the halo gas probed by Mg II lines is approximately aligned with the galaxy's angular momentum vector, which suggests that the Mg II gas co-rotates with galaxy disks. Using the same catalog of Mg II absorbers, Schroetter et al. (2019) selected 26 quasar–galaxy pairs and studied their azimuthal angle, which is the angle between the galaxy's major axis and quasar location (see e.g., Zabl et al. 2019 Figure 1). The bimodality of azimuthal angles suggests that the outflows are bi-conical in nature.

Strong Mg II systems, defined by their rest-frame equivalent width W_r , are found to trace cosmic star formation rate (SFR; Ménard et al. 2011). Observations have shown that Mg II absorbers are associated with a large amount of neutral gas (Lanzetta et al. 1987; Steidel et al. 1995, 1997; Rao et al. 2006; Nestor et al. 2007). Rao et al. (2006) studied 197 Mg II systems and their H I profiles at 0.11 < z < 1.65 using Hubble Space Telescope (HST) UV spectroscopy. Their results show that all the damped Ly α (DLA) systems (log N(H I) [cm⁻²] > 20.3) have W_r (λ 2796) > 0.6 Å. As DLA systems are regarded as the progenitors of star-forming galaxies today, consequently, strong Mg II absorption systems are thought to be correlated with star formation as well. As pointed out in Matejek & Simcoe (2012, hereafter M12), systems traced by strong Mg II absorbers tend to belong to galaxies with high SFRs. In the

literature, some studies define systems with $W_r(\lambda 2796) > 0.3 \text{ Å}$ as strong systems, while others use $W_r(\lambda 2796) > 1.0 \text{ Å}$. In this paper, we use the latter as the definition of strong Mg II absorbers.

To trace star formation with strong Mg II absorption systems, the first parameter to calculate is the pathlength number density. The pathlength can be redshift (dz) or comoving pathlength (dX), for which

$$X(z) = \int_0^z (1+z')^2 \frac{H_0}{H(z')} dz. \tag{1}$$

The number of absorbers per unit redshift (per absorption distance) dN/dz (dN/dX) has been studied in strong Mg II systems at low to high redshift. The evolution of the comoving line density dN/dX is above and beyond passive evolution due to the expansion of the universe. At z < 2, Zhu & Ménard (2013) found that the dN/dz of Mg II absorbers rises with increasing redshift. At z > 2, M12) and Chen et al. (2017; hereafter C17) show that the comoving dN/dz of strong Mg II ($W_r > 1$ Å) decreases with increasing redshift, by analyzing 110 absorbers at $1.98 \le z \le 5.3$. In contrast, the comoving dN/dz of weak Mg II systems with $W_r(\lambda 2796) < 1$ Å is nearly constant over cosmic time (Nestor et al. 2005; M12; Chen et al. 2017), which is quite different from that of strong systems.

In this paper, we present a sample of strong Mg II absorbers detected in the near-IR spectra of 31 quasars at z > 5.7 and study the evolution of their number density at 2.2 < z < 6.0. We also explore possible connections between the absorbers and properties of the associated galaxies. This paper is presented as follows. We introduce our sample and absorption detection method in Section 2. The results are presented in Section 3. We discuss possible galaxy counterparts in Section 4. Throughout the paper, all magnitudes are expressed in the AB system. The standard cosmology parameters are used: $H_0 = 70 \, \mathrm{km \, s^{-1} \, Mpc^{-1}}$, $\Omega_{\Lambda} = 0.7 \, \mathrm{and} \, \Omega_m = 0.3$.

2. Data and Detection of Mg II Absorbers

The quasar near-IR spectra used in this paper were from a large Gemini-GNIRS program (Shen et al. 2019). Shen et al. observed most of the 52 quasars at z > 5.7 (Jiang et al. 2016) and this program was carried out during 15B-17A semester. By excluding those quasars that already have reasonable good quality spectra, the final sample consists of 50 quasars. Most of these 50 quasars were initially selected from Sloan Digital Sky Survey (SDSS) with a color cut of i - z > 2.2 and have no detection in *ugr* bands (Jiang et al. 2016). The observations were executed using the standard ABBA method. A crossdispersion mode was used to cover the wavelength range from 0.85 to $2.5 \mu m$. We use a slit width of 0.675 that delivers a resolving power $R \sim 800 \ (\sim 376 \, \mathrm{km \, s^{-1}}; \ \mathrm{GNIRS} \ \mathrm{mean}$ resolution) with a pixel scale of 0".15"/pix. The spectral resolution is estimated from the average FWHM of weak and unblended emission lines in the arc file. The emission redshifts of quasars in the sample were measured from a series of lines (Mg II, C III], Si III, Al III, C IV, He II, O III], Si IV), which takes the velocity shifts of each line into account (Shen et al. 2019). The updated redshifts may differ from the original redshifts in the discovery papers, which are with optical spectra only (see Table 1). The median emission redshift uncertainty is $\sim 300 \, \mathrm{km \, s^{-1}}$. The GNIRS data were reduced by the combination of two pipelines, PyRAF-based

XDGNIRS (Mason et al. 2015) and the IDL-based XIDL package. The details are described in Shen et al. (2019).

We clarify that the quasar colors in our sample are consistent with that at lower redshift, hence, there is very limited bias caused by the background quasars for absorption candidates selection. Color bias of the background quasars in large samples would possibly affect the foreground absorbers selection. For example, in Prochaska et al. (2009), they found an elevated incidence of Lyman limit opacity in the intergalactic medium. This is related to the SDSS quasar selection bias at z=3.5 to z=3.6. Considering our sample size and quasar colors, this effect, if any, would be within errors and not affect significantly the absorption study results. Also, we did not select absorption candidates based on any presumptions of N (H I). The selection process of absorption candidates is presented in details in Section 2.1.

2.1. Detection Algorithm

We selected 31 quasars with signal-to-noise ratios (S/N)greater than 10. The S/N is a mean S/N per resel measured from the "clean" continuum region of the spectra without strong OH skylines or water vapor absorption features. The mean S/N values of all spectra are presented in Table 1. Given the low resolution ($R \sim 800$) of GNIRS spectra, we did not use the lower S/N spectra. We first fitted each quasar spectrum with a continuum. The continuum was selected interactively with knots in the absorption-free wavelength region. The region between two knots was fitted with a spline curve. Then the spectrum was normalized with this continuum. We then used our algorithm to automatically search and identify metal absorbers in the normalized spectra. The absorption feature was identified with a Gaussian kernel filter, which has a rest-frame velocity FWHM between 376 km s⁻¹ and 600 km s⁻¹ (six pixels, empirically selected). If W_r of this Gaussian kernel were greater than 0.8 Å, which is our detection limit (e.g., observe equivalent width \sim 3 Å around wavelength 10,000 Å) for Mg II line, then it was considered as an absorption feature. The W_r was measured from the flux summation over $\Delta\lambda$ where the Gaussian kernel is within 3% of the continuum. For Mg II doublet, the two kernels of the doublet are separated by \sim 770 km s⁻¹ and cross-correlated with the spectrum simultaneously. The selection criteria of Mg II candidates relate to W_r , $\sigma(W_r)$ and S/N in the continuum. We calculated the $\sigma(W_r)$ by using a method by Vollmann & Eversberg (2006). For a normalized spectrum, the W_r of an absorption line is defined as:

$$W_r = \int_{\lambda_2}^{\lambda_1} (1 - F) d\lambda \approx \Delta \lambda_r (1 - \overline{F}), \tag{2}$$

where $\Delta \lambda_r = (\lambda_2 - \lambda_1)/(1+z)$ is the rest-frame absorption line width. \overline{F} is the mean normalized flux density of the absorption line. Equation (2) can be expanded in a Taylor series:

$$W_r = W_r(\overline{F}) + \frac{\partial W_r}{\partial \overline{F}} \sigma(F).$$
 (3)

According to Equation (2), there is $\frac{\partial W_r}{\partial F} = -\Delta \lambda$. Together with $\sigma(F) = \frac{\overline{F}}{S/N_c}$, we have

$$\sigma(W_r) = \Delta \lambda \times \frac{\overline{F}}{(S/N)_c}.$$
 (4)

Table 1Summary of 32 Strong Absorbers

(1) Quasar	(2) z_{em}	(3) z_{abs}	(4) W _r (λ2796) (Å)	(5) $W_r(\lambda 2803)$ (Å)	(6) $W_r(\lambda 2600)$ (Å)	$ (7) \ \Delta v (km \ s^{-1}) $	$ (8) \ \Delta v_{\rm obs} (km \ s^{-1}) $	(9) S/N
P000+26	5.733	3.708	1.05 ± 0.28	0.90 ± 0.23		<152	<435	18
J0002+2550	5.818	3.059	1.92 ± 0.38	1.86 ± 0.16		478 ± 38	707 ± 22	18
J0008-0626	5.929			•••				10
J0028+0457	5.982	4.845	2.24 ± 0.76	1.65 ± 0.58		379 ± 37	717 ± 20	10
		3.282	1.51 ± 0.48	1.76 ± 0.49	0.91 ± 0.43	232 ± 36	640 ± 18	
J0050+3445	6.251	3.435	3.44 ± 0.88	2.02 ± 0.56	1.05 ± 0.39	609 ± 39	820 ± 24	10
J0203+0012	5.709							16
J0300-2232	5.684	4.100	2.06 ± 0.86	1.51 ± 0.63	0.67 ± 0.32	353 ± 37	690 ± 20	13
J0353+0104	6.057							13
J0810+5105	5.805		•••				•••	13
J0836+0054	5.834	3.745	2.46 ± 0.44	1.84 ± 0.42	0.66 ± 0.29	548 ± 39	785 ± 24	20
J0840+5624	5.816	5.595	2.74 ± 0.25	2.57 ± 0.10	0.00 ± 0.29 0.71 ± 0.28	194 ± 36	661 ± 18	17
J0842+1218	6.069	5.050	1.66 ± 0.57	1.25 ± 0.36	2.04 ± 0.54	316 ± 37	660 ± 20	13
30042+1210	0.007	2.540	2.68 ± 0.51	1.75 ± 0.73	0.90 ± 0.36	310 ± 37 310 ± 37	661 ± 20	13
		2.392	2.08 ± 0.31 2.01 ± 0.30	1.73 ± 0.73 1.91 ± 0.24	1.21 ± 0.50	334 ± 37	709 ± 20	
J0850+3246	5.730	3.333					494 ± 20	17
JU83U+3240	3.730	3.333	1.65 ± 0.46	1.18 ± 0.32	1.15 ± 0.33	165 ± 37		17
10027 + 2001	5 770		1.10 ± 0.34	0.38 ± 0.35	1.03 ± 0.38	200 ± 37	440 ± 20	10
J0927+2001	5.770							10
J1044-0125	5.780	2.278	2.01 ± 0.31	1.76 ± 0.32	0.71 ± 0.23	155 ± 34	398 ± 14	19
J1137+3549	6.009	5.013	1.73 ± 0.57	1.32 ± 0.45	0.96 ± 0.48	481 ± 38	702 ± 22	10
J1148+0702	6.344	4.369	4.23 ± 0.52	2.88 ± 0.43	3.61 ± 0.54	410 ± 38	690 ± 22	12
		3.495 ^a	6.50 ± 1.20	6.3 ± 0.70	1.64 ± 0.46	>865	>1059	13
J1148+5251	6.416	6.009	1.10 ± 0.34	0.75 ± 0.27	1.63 ± 0.18	207 ± 38	611 ± 22	18
		4.944	1.24 ± 0.46	1.21 ± 0.42	0.34 ± 0.29	<103	<613	
		3.557	1.62 ± 0.30	1.74 ± 0.21	0.74 ± 0.25	349 ± 35	400 ± 16	
J1207+0630	6.028	3.808	1.63 ± 0.40	1.50 ± 0.45	1.66 ± 0.47	456 ± 36	663 ± 18	10
J1243+2529	5.842		•••	•••	•••	•••	•••	11
J1250+3130	6.138	4.201	3.06 ± 0.52	2.68 ± 0.51	0.73 ± 0.52	179 ± 38	530 ± 22	12
		3.860	1.78 ± 0.60	1.01 ± 0.49	1.80 ± 0.58	297 ± 35	630 ± 16	
		2.292	2.37 ± 0.42	1.92 ± 0.47	•••	381 ± 37	699 ± 20	
J1257+6349	5.992	•••	•••	•••	•••	•••	•••	11
J1335+3533	5.870	4.530	1.21 ± 0.45	1.27 ± 0.30	1.33 ± 0.47	323 ± 38	545 ± 22	15
J1425+3254	5.862	3.136	1.08 ± 0.39	1.12 ± 0.58	1.04 ± 0.32	171 ± 38	507 ± 22	14
		3.001	1.22 ± 0.62	0.92 ± 0.65	1.10 ± 0.46	170 ± 38	503 ± 22	
J1429+5447	6.119							12
J1545+6028	5.794	4.152	2.32 ± 0.35	2.03 ± 0.23	0.65 ± 0.21	191 ± 36	475 ± 18	20
		3.616	2.03 ± 0.49	1.05 ± 0.50	0.79 ± 0.42	160 ± 35	564 ± 16	
J1602+4228	6.083		•••		•••	•••	•••	13
J1609+3041	6.146	3.896	1.33 ± 0.23	1.54 ± 0.27	1.66 ± 0.23	132 ± 35	391 ± 16	12
J1621+5155	5.637		•••	•••	•••			20
J1623+3112	6.254							12
J2310+1855	5.956	4.244	1.86 ± 0.35	0.98 ± 0.21	1.90 ± 0.25	221 ± 34	555 ± 14	18
		4.013	1.19 ± 0.21	1.20 ± 0.26	0.83 ± 0.33	<165	<388	

Note. (1) Quasars. (2) Emission redshift of the quasars. (3) Absorption redshift of Mg II systems, measurement errors of z_{abs} are smaller than 0.001. (4) Equivalent widths of Mg II (λ 2796) lines, which are from a Voight profile. The errors are measured by the method introduced in Section 2.1.; same for columns (5) and (6). (5) Equivalent width of Mg II (λ 2803) lines. (6) Equivalent width of Fe II (λ 2600) lines. (7) Velocity width of Mg II (λ 2796) lines. Instrument broadening was removed. The error of $\Delta \nu$ was computed from the quadratic sum root of 1σ error of FWHM_{arc} and FWHM_{obs}, which are FWHMs of arc files and observed absorption profiles. (8) Observed velocity width of Mg II (λ 2796) lines. (9) Mean S/N of the spectra.

 $(S/N)_c$ is the average S/N per resel of ± 10 pixels adjacent to $\Delta \lambda$. The specific Mg II candidates selection criteria are in the following:

- (1) $W_r(\lambda 2796) / \sigma(W_r) > 3$.
- (2) $W_r(\lambda 2796) > 0.8 \text{ Å} \text{ and } W_r(\lambda 2803) > 0.4 \text{ Å},$
- (3) S/N > 3 per resel in three or more contiguous pixels beyond the $\Delta \lambda$ region.

We searched for Mg II systems in all 31 quasar spectra using the above criteria and obtained 110 candidates.

Afterward, at least two Fe II lines (at 1608, 1611, 2344, 2374, 2586, or 2600 Å) were visually inspected at the same redshift to further confirm the identified Mg II doublet. In the end, we confirmed 32 Mg II and Fe II absorbers at 2.2 < z < 6.0. The spectra of the absorbers are presented in Figure 1. We found that all these Mg II absorbers have $W_r(\lambda 2796) > 1.0$ Å, and 13 of them are very strong with $W_r(\lambda 2796) > 2.0$ Å. The median W_r is 1.86 Å. The redshift distribution (with a median z = 3.743) of these absorbers is shown in Figure 2.

^a This Mg II doublet is strongly blended, so measurements have inevitably large uncertainties.

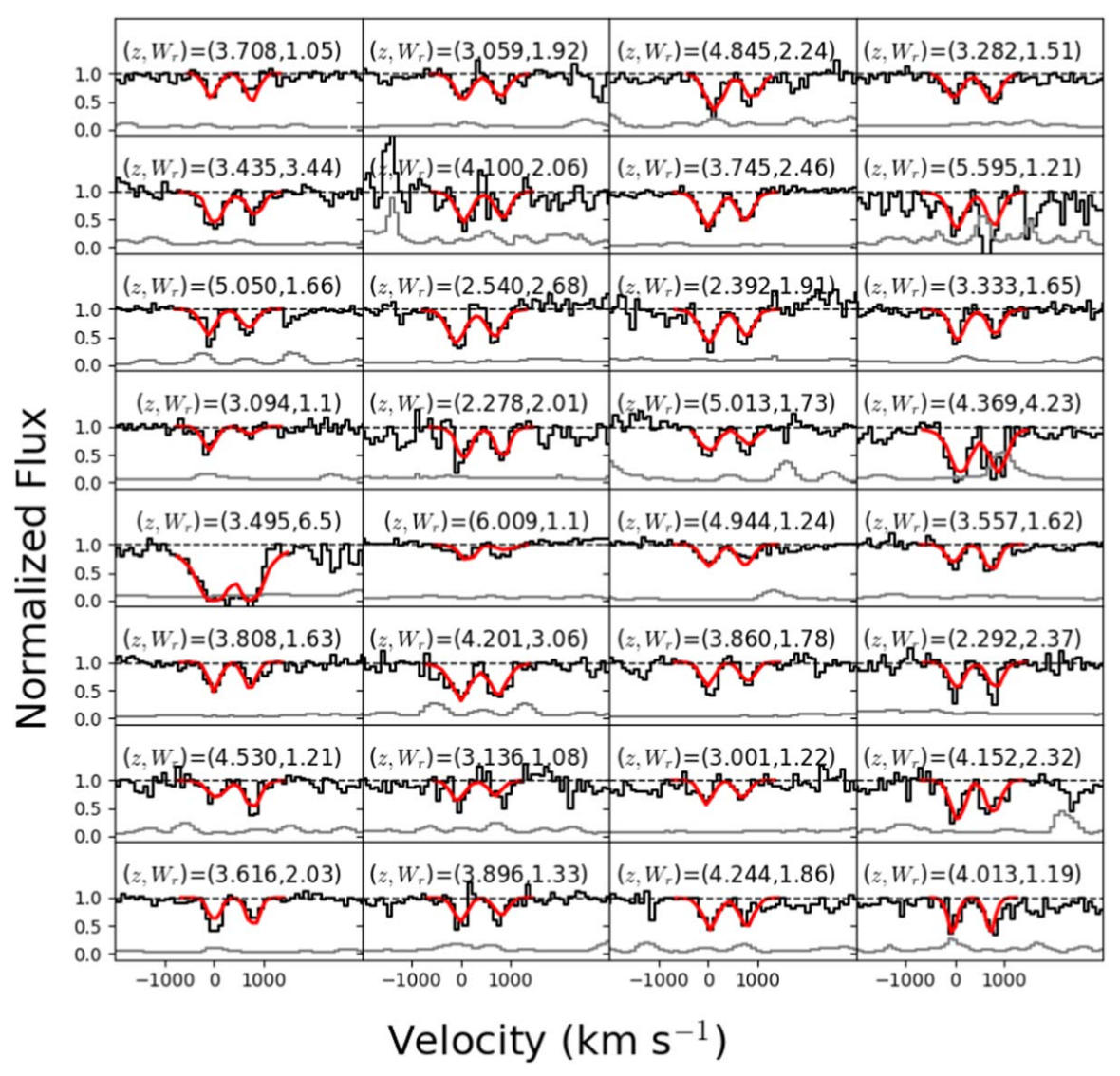


Figure 1. All strong Mg II absorbers in this work. Absorption line redshift z and W_r (Å) are labeled for each absorber. The median W_r for the all the Mg II absorbers is 1.78 Å and median absorbers redshift is z = 3.743. The black and gray curves are the normalized spectra and noise spectra, respectively. The red curves are the best-fitted Voigt profiles. Each absorber is centered at the absorption profile of Mg II $\lambda 2796$.

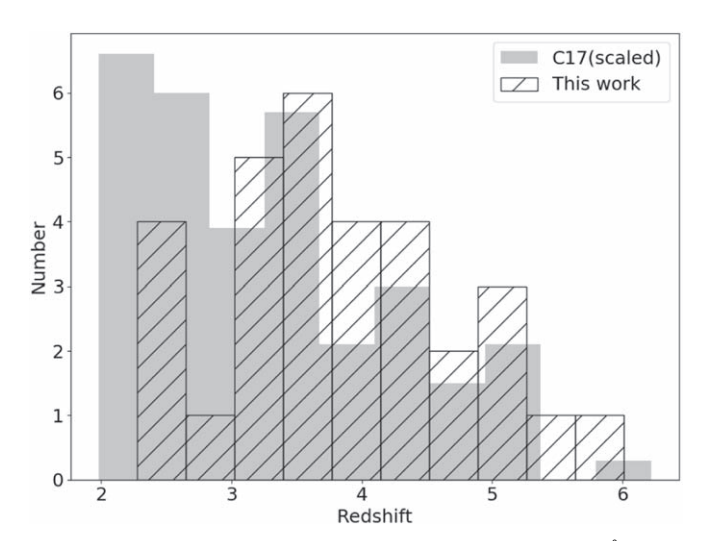


Figure 2. Redshift distribution of strong Mg II absorbers $(W_r > 1 \text{ Å})$ in this work (hashed). The redshift distribution of Chen et al. (2017) is scaled by a factor of 0.30 for comparison (in gray).

2.2. Measurements

We also measured W_r of an absorption candidate from a Voigt profile fit. The line is fitted using the VoigtFit package (Krogager 2018). During the visual inspection process, we noticed that our detection algorithm detected a few absorbers as candidates but they are strongly blended, e.g., Mg II (λ 2803) lines at z = 3.059 (J0002+2550), z = 5.595 (J0840+5624), z = 4.201 (J1250+3130), and z = 4.530 (J1335+3533). Due to this blending, the W_r would be overestimated from the flux boxcar summation. The Doppler parameter b values of the fits are between 20-60 km s⁻¹. Because the relatively low resolution would introduce large uncertainties on the b and column density measurements, we only use Voigt fits to calculate the W_r , which is independent of spectral resolution. We compared the measurements from the fits and the flux summation. Except for systems with obvious blending, the differences between the two measurements have a median of 0.13 Å and a maximum of 0.5 Å.

We then measured the velocity width from the best-fitted parameters. The intrinsic rest-frame velocity width Δv was

determined by the instrument broadening and observed velocity width $\Delta\nu_{\rm obs}$. The observed $\Delta\nu_{\rm obs}$ was measured between the leftmost and rightmost pixels with optical depth $\tau<0.1$. The optical depth τ equals ln (1/F), where F is the normalized flux at this wavelength. This measurement is similar to the standard $\Delta\nu_{90}$ definition (Prochter et al. 2006). The idea is to include all satellite absorption and to have a good representation of the kinematic extent of the absorption. We measured instrument broadening from lamp/arc lines used for wavelength calibration. The average FWHM of the arc lines FWHM $_{\rm arc}$ is roughly 376 \pm 31 km s $^{-1}$ (with 1σ error). The rest-frame intrinsic FWHM was calculated by FWHM = $\sqrt{\rm FWHM_{obs}}^2 - \rm FWHM_{arc}^2/(1+z)$, where FWHM $_{\rm obs}$ is the observed FWHM of the line. Then we assume the ratio of intrinsic FWHM and $\Delta\nu$ is the same as the ratio of observed FWHM and $\Delta\nu_{\rm obs}$, i.e., $\Delta\nu={\rm FWHM}\times(\Delta\nu_{\rm obs}/{\rm FWHM_{obs}})$.

To minimize the low resolution impact on our velocity spread measurements, we create 50 mock Mg II absorption spectra and convolved them into FIRE resolution of R=6000 (i.e., $50 \, \mathrm{km \, s^{-1}}$) and GNIRS resolution of $R \sim 800$ (i.e., $376 \, \mathrm{km \, s^{-1}}$), respectively. Then we measured the Δv from the mock spectra with different resolutions using the same method described above. The measurements are consistent within errors $\sim 20 \, \mathrm{km \, s^{-1}}$ (see Figure 3). We also used a FIRE spectra of Fe II ($\lambda 2374$) system at z=3.495 toward QSO J0148 +0702. We degraded the spectral resolution into R=800. The velocity width measurement difference between the original and degraded spectra is within $30 \, \mathrm{km \, s^{-1}}$.

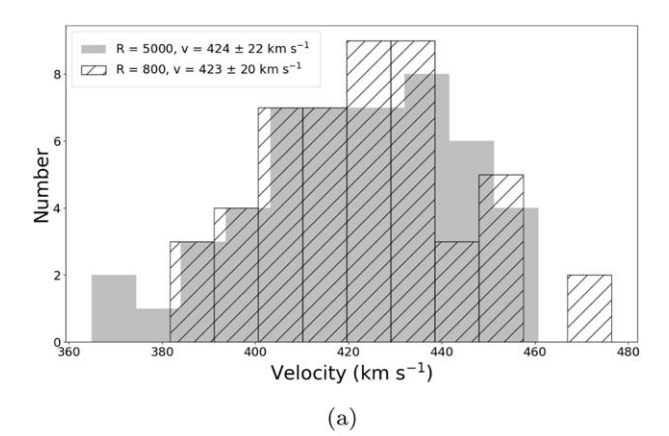
The intrinsic and observed velocity widths of all the detected absorbers are shown in Table 1's columns (7) and (8), respectively. We found that 15 out of 32 absorbers have $\Delta v > 300 \, \mathrm{km \, s^{-1}}$. We fit the relation between Δv and W_r using a polynomial curve fitting technique considering the errors from two variables (see Figure 4).

$$\Delta v = 75.63 \text{ km s}^{-1}\text{Å}^{-1} \times W_r + 141.19 \text{ km s}^{-1}.$$
 (5)

2.3. Comparison with C17

We compared measurements of five overlapping sightlines (J0203+0012, J0836+0054, J0842+1218, J1148+0702, and J2310+1855) between our sample and the FIRE sample in C17. The details are presented in the following and Table 2.

All Mg II systems in J0203+0012 and the one at z = 2.299toward J0836+0054 reported in C17 are below 1 Å, which are beyond our detection limit. The W_r , Δv and z measurements of the system at z = 3.745 toward J0836+0054 are consistent. For J0841+1218, three systems were detected in this work and C17 at z = 5.050, 2.540, 2.392. The W_r , Δv and z measurements are consistent with errors. For J1148+0702, we detected two systems at z = 4.369 $(W_r(\lambda 2796) = 4.23 \pm 0.52 \text{ Å})$ and z = 3.495 $(W_r(\lambda 2796) = 6.50 \pm 1.20 \,\text{Å})$. The measurements of the system at z = 4.369 are consistent with that in C17. The system at z = 3.495 has extremely large velocity width (>800 km s⁻¹ for Mg II (λ 2796) line) and the absorptions are strongly blended within the doublet. Thus, the W_r and Δv measurements of this system inevitably have large uncertainties. We did not use this measurement when calculating the relation in Equation (5). For J2310+1855, the two systems at z = 3.299 and 2.351 detected in C17 have $W_r < 1.0$ Å, which are beyond our detection ability. The one at z = 2.243 is located in a noisy region where the lines are not able to be detected in our spectrum. We detected two systems at z = 4.244 and z = 4.013, which are not included



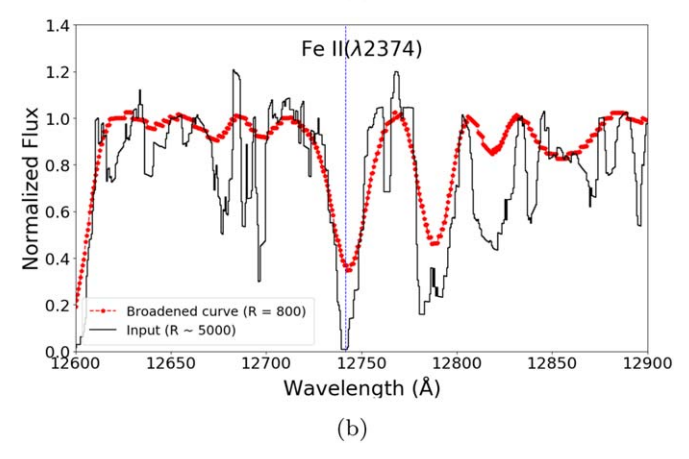


Figure 3. (a). Velocity widths (Δv) histogram of 50 mock Mg II doublets spectra with R=800 (hashed) and R=6000 (gray), respectively. Definition and measurement of Δv are described in Section 2.2. The R=6000 spectra are Voigt profiles with FWHM = 270 km s⁻¹. Then they were convolved into R=800. Noise was added with a normal distribution and S/N was set to 10. The median Δv measured with the method described in Section 2.2 for R=800 and R=6000 spectra are 423 ± 20 km s⁻¹ and 424 ± 22 km s⁻¹. (b). Fe II ($\lambda 2374$) line at z=3.495 toward J1148+0702 from a Megellan-FIRE Spectrum. The input spectral resolution is around 6000 (black curve). The broadened red curve is the resolution–convoluted spectra with R=800. Velocity widths measured with input and broadened spectra are 566 km s⁻¹ and 531 km s⁻¹, respectively.

in C17. The first one has $W_r(\lambda 2796) = 1.86 \pm 0.35 \text{ Å}$ and $\Delta v = 221 \pm 34 \text{ km s}^{-1}$. The second one has $W_r(\lambda 2796) = 1.19 \pm 0.21 \text{ Å}$ and $\Delta v < 165 \text{ km s}^{-1}$ (see the last two panels in Figure 1). The system at z = 4.244 was present in an inspection of the spectrum used in C17, but was rejected by their automated search algorithm because $W_r(\lambda 2803) > W_r(\lambda 2796)$, likely because of blending in the Mg II ($\lambda 2803$) line from interloping systems at lower redshift. The system at z = 4.013 has severe telluric noise in FIRE spectrum (R. Simcoe 2020, private communication).

In summary, except for the systems where $W_r(\lambda 2796) < 1 \text{ Å}$ or where the spectra S/N is too low, our absorption redshift, equivalent width and velocity spread measurements are consistent with that in C17, within errors. Though it is possible that, for systems where $\Delta v_{\rm obs} < 400 \, {\rm km \, s^{-1}}$ (close to GNIRS resolution), our velocity widths uncertainties would be large.

3. Results

The near-IR spectra are strongly contaminated by OH skylines and telluric absorption. To conduct population

Table 2

Measurements of the Overlapping Sightlines Between This Work and C17

(1) Quasar	(2) z _{abs}	(3) <i>W_r</i> (λ2796) GNIRS (Å)	(4) <i>W_r</i> (λ2796) C17 (Å)	$(5)\Delta v$ GNIRS (km s^{-1})	(6) $\Delta v \text{ C17}$ (km s ⁻¹)
J0836+0054	3.745	2.46 ± 0.44	2.51 ± 0.02	548 ± 39	510.4
J0842+1218	5.050	1.66 ± 0.57	1.81 ± 0.15	301 ± 37	245.1
	2.540	2.68 ± 0.51	2.16 ± 0.10	310 ± 37	384.5
	2.392	2.01 ± 0.30	1.44 ± 0.25	279 ± 37	193.8
J1148+0702	4.369	4.23 ± 0.52	4.78 ± 0.11	410 ± 38	371.9
	3.495	6.50 ± 1.20	4.82 ± 0.19	>865	899.2
J2310+1855	4.244	1.86 ± 0.35		221 ± 34	
	4.013	1.19 ± 0.21		<165	

Note. J0203+0012 is not in this table, because the W_r measurements of all systems detected in C17 are beyond our detection limit. (1) Quasars. (2) Mg II absorption redshifts. (3) Rest-frame equivalents of Mg II (λ 2796) measured in GNIRS. (4) Rest-frame equivalents of Mg II (λ 2796) in C17. (5) Velocity widths measured in GNIRS. (6) Velocity widths measured in C17.

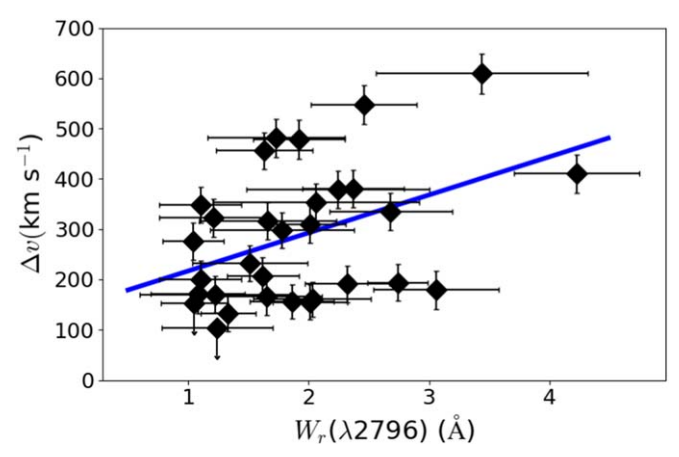


Figure 4. Mg II (λ 2796) velocity width (Δv) against rest-frame equivalent width (W_r). The blue line is the linear relation of our sample with 2σ limit: 75.63 km s⁻¹ Å⁻¹ × W_r + 141.19 km s⁻¹ in Equation (5).

statistics analysis for absorbers, we need to correct the incompleteness caused by the contamination. In this section, we first correct these effects and then present the statistical dN/dz and dN/dX for our Mg II sample.

3.1. Completeness

For each quasar spectrum, we performed a Monte Carlo simulation by inserting uniformly distributed, virtual Mg II doublets in the wavelength range between 8500 Å and 20,000 Å, corresponding to the absorber redshift of 2.0 and 6.2, respectively. The inserted $W_r(\lambda 2796)$ varies between 1.0 and 4.5 Å, which is the observed W_r range of our detected Mg II absorbers (except for the strongly blended one toward J1148+0702). For each W_r , its velocity width follows the relation $\Delta v = 103.37 \text{ km s}^{-1} \text{ Å}^{-1} \times W_r + 399.60 \text{ km s}^{-1}$, which we measured from the $\Delta v_{\rm obs}$ and W_r . Two strong water vapor regions $(1.35-1.42 \,\mu\mathrm{m}$ between J and H and $1.82-1.93 \mu m$ between H and K band) are discarded in the statistical analysis of dN/dz and dN/dX. Then we use the algorithm introduced in Section 2.1 to detect the inserted virtual absorbers. We measured the uncertainties between inserted and retrieved measurements from 1000 mock inserted Mg II systems. The measurement errors of W_r and z are 0.015 Å and 0.002, respectively (see Figure 5). This bias would be affect the final completeness significantly. The detection

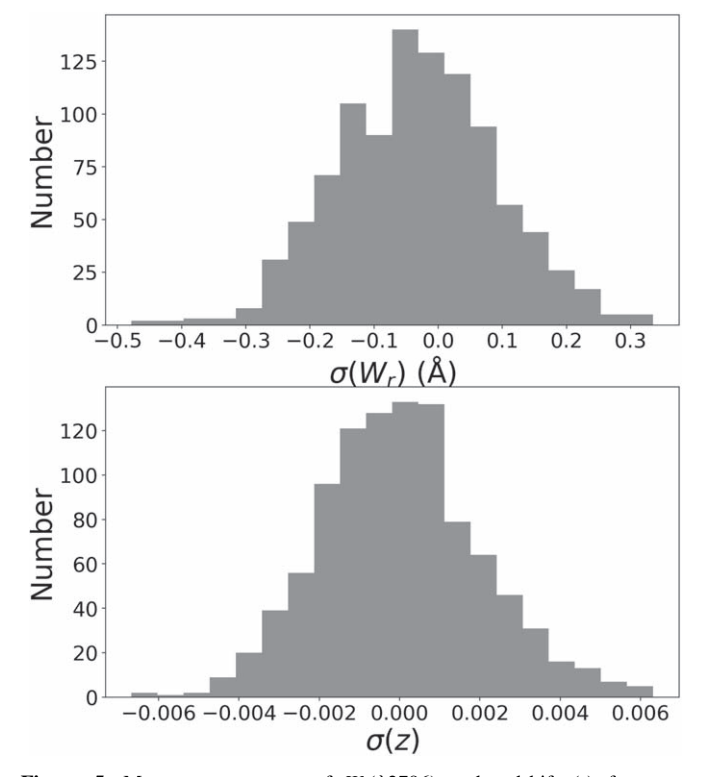


Figure 5. Measurement errors of $W_r(\lambda 2796)$ and redshift (z) from our simulation. The errors of W_r and z are 0.15 Åand 0.002, respectively. The errors were calculated by comparing the inserted and measured values of 1000 mock Mg II absorbers.

result is denoted as a Heaviside function $H(z, W_r)$:

$$H(z, W_r) = \begin{cases} 1, & \text{if the absorber is detected,} \\ 0, & \text{if the absorber is not detected.} \end{cases}$$
 (6)

The redshift-weighted density $g(z, W_r)$ is a function of W_r and z denoted as

$$g(z, W_r) = \sum_{i=1}^{N} H(z, W_r),$$
 (7)

where N is the total number of sightlines. The total path g(z) is obtained as the integral of the path density over the whole

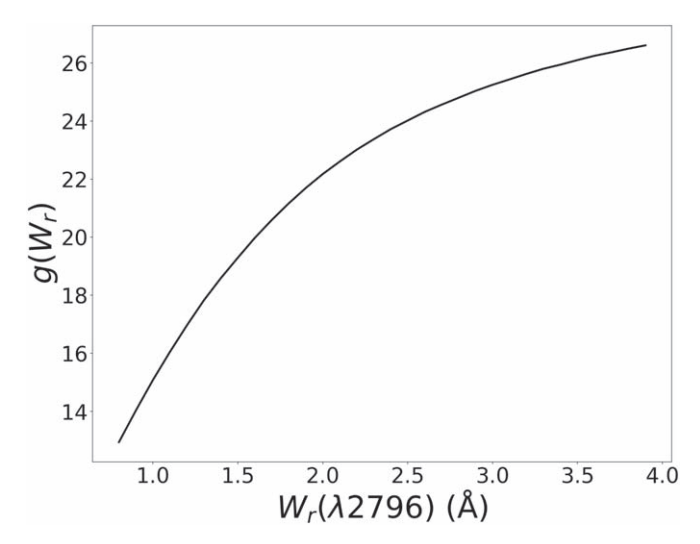


Figure 6. Total absorption path $g(W_r)$ against rest-frame equivalent width W_r .

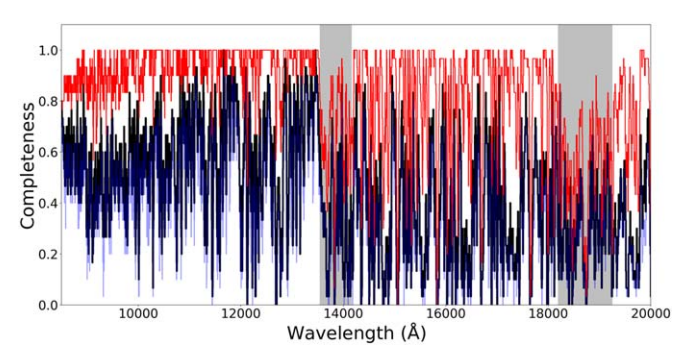


Figure 7. Average pathlength-weighted completeness $\overline{C}(W_r,z)$ for 31 sightlines in the sample with $W \geqslant 0.8$ (light blue), 1 (black) and 3 Å (red), respectively. Two strong water vapor regions are labeled with vertical gray regions.

range that we selected (see Figure 6):

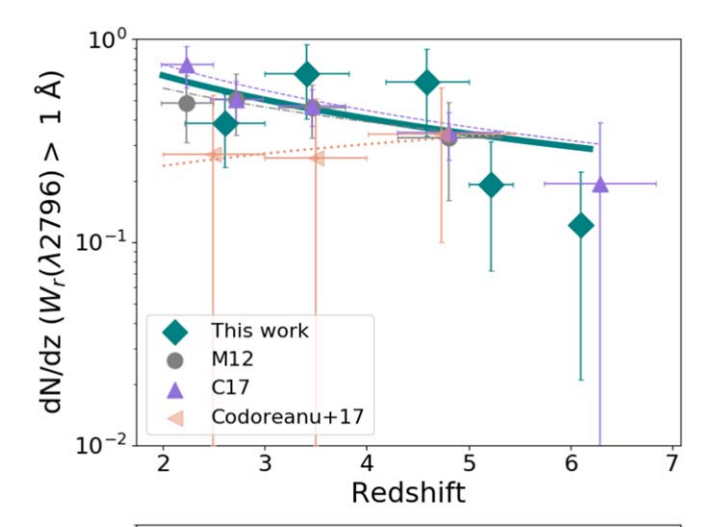
$$g(z) = \int_{W_0}^{\infty} g(z, W_r) dz, \tag{8}$$

where W_0 is the W_r limit. For each sightline, its completeness is the detection rate of the inserted absorbers. The completeness of pathlength is a function of redshift and W_r ,

$$C(z, W_r) = g(z, W_r)/N.$$
(9)

We show the pathlength-averaged completeness $\overline{C}(z, W_r)$ for the selected 31 sightlines with $W_r(\lambda 2796) > 0.8$ Å, 1 Å and >3 Å in Figure 7. For $W_r(\lambda 2796) > 1$ Å the completeness is around $40\% \sim 80\%$ in the J band $(1.17-1.37 \ \mu\text{m})$, and around $20\% \sim 60\%$ in the H band $(1.49-1.80 \ \mu\text{m})$. The low completeness in the H band is due to the contamination of strong skylines.

Even if the S/N of a spectrum is high enough to detect weak lines, visual inspection may miss some weak absorbers. The probability for users to confirm true absorbers is defined as user acceptance. In M12 and C17, the user acceptance rate is defined as a function of S/N and has been considered in their calculations. M12 suggests that when S/N > 10, the user acceptance is close to 1 and the rejection fraction of false-positive candidates is close to 0.



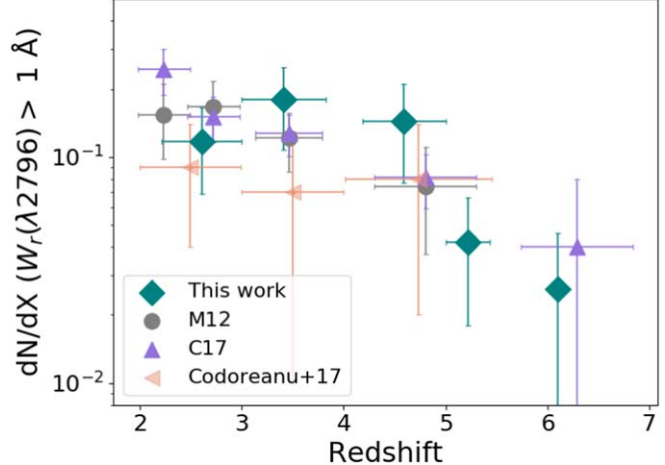


Figure 8. Line density dN/dz (upper panel) and comoving line density dN/dX (lower panel) of the Mg II absorbers in our sample. Our results are plotted as green curves and diamonds. The purple triangles are the data from Chen et al. (2017) and the gray dots represent data of M12. The orange triangles represent a sample of Codoreanu et al. (2017). The relation presented by M12 is (in purple) $dN/dz = (1.301 \pm 1.555) \times (1 + z)^{-0.746 \pm 0.857}$. Relation in C17 is (in gray) $dN/dz = (2.298 \pm 1.561) \times (1 + z)^{-1.020 \pm 0.475}$. The orange dashed line is relation in Codoreanu et al. (2017): $dN/dz = (0.14 \pm 0.09) \times (1 + z)^{0.48 \pm 0.20}$.

Zhu & Ménard (2013) identified 40,000 Mg II absorbers from SDSS at 0.4 < z < 2.3. By requiring the simultaneous detection of Fe II lines ($\lambda\lambda 2344$, 2383, 2586, 2600) for each Mg II absorption line, they recovered close to 100% of strong absorbers in the Pittsburgh catalogs (Quider et al. 2011). In this work, we focus on the strong system with $W_r(\lambda 2796) \ge 1$ Å, for which we also confirm detection of Fe II candidate lines at the same absorption redshift. Given this and that our database consists of spectra with S/N > 10, we assume that our visual inspection is correct at a rate of ca 95%. In the case that one or two Fe II candidate lines reside in the water vapor region and are affected significantly by OH lines, the bias would be within this rate given the wide wavelength coverage of Fe II candidate lines. We calculated the Fe II lines association with strong Mg II systems in M12. We found that there are 35 out of 37 (94.5%) strong Mg II systems ($W_r(\lambda 2796) > 1 \text{ Å}$) associated with at least three clear Fe II lines. Additionally, spurious detection caused e.g., by C IV doublets $W_r(\lambda 1548 > 0.5 \text{ Å})$, are not detected in our spectra. Therefore, the false-positive detection rate from the weaker lines is close to 0.

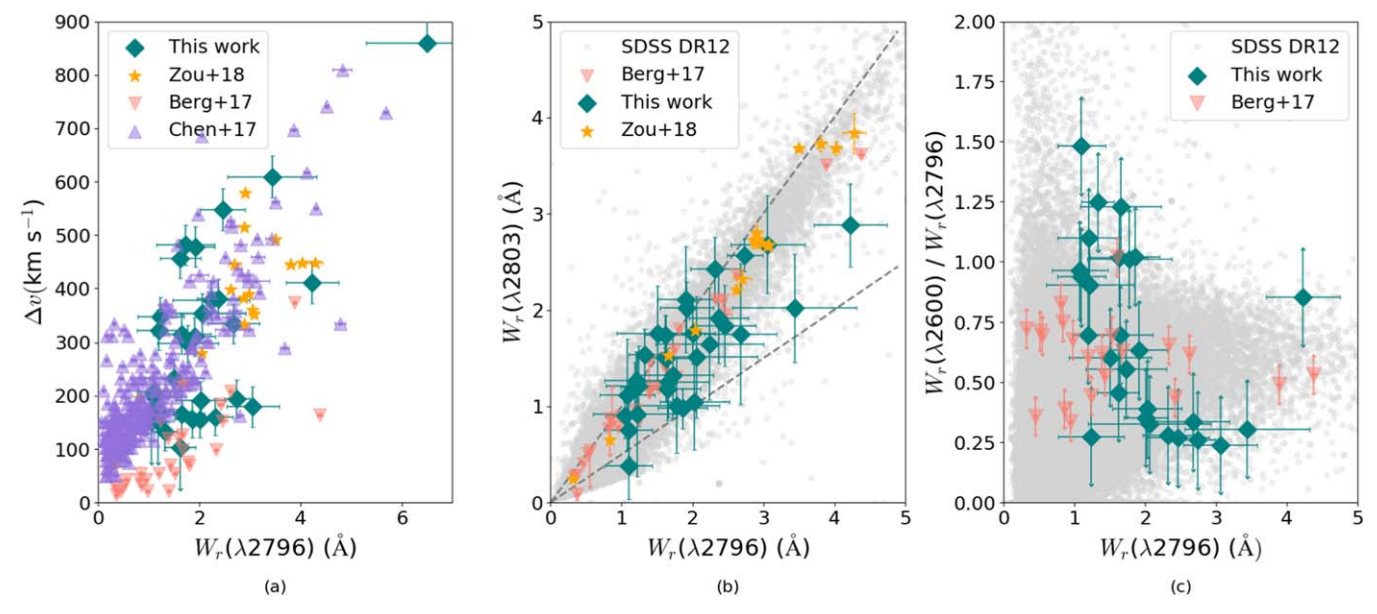


Figure 9. Properties of the absorbers in our sample and comparison with previous studies: an SDSS sample of Mg II systems z < 2 from Zhu & Ménard (2013), a sample of DLA–Mg II systems from XQ-100 survey (Berg et al. 2017), and a sample of Mg II associated with neutral atomic carbon (C I) absorbers in Zou et al. (2018). (a) Velocity width Δv against $W_r(\lambda 2796)$. The purple triangles are the data from C17. Our Mg II systems are very likely affected by galactic superwinds. (b) $W_r(\lambda 2803)$ - $W_r(\lambda 2796)$ relation for different samples. The two dashed line represents the ratio of $W_r(\lambda 2803)/W_r(\lambda 2796) = 1.0$, 0.5, respectively. Our Mg II lines exhibit potentially less saturation than other two samples. (c) Ratio of $W_r(\lambda 2600)/W_r(\lambda 2796)$ against $W_r(\lambda 2796)$. Our strong Mg II systems show relatively smaller $W_r(\lambda 2600)/W_r(\lambda 2796)$ ratios, one possible reason is that Mg II clouds at higher redshift are in the interactions of multiple unresolved subcomponents.

 Table 3

 Pathlength Density of Mg II Absorbers

$(1) \Delta z$	(2) \overline{C} (%)	(3) dN/dz	(4) dN/dX		
2.220–3.000	47.1	0.386 ± 0.153	0.117 ± 0.048		
3.000-3.828	49.6	0.672 ± 0.268	0.179 ± 0.071		
4.185-5.000	29.7	0.612 ± 0.280	0.144 ± 0.067		
5.000-5.436	31.6	0.192 ± 0.120	0.042 ± 0.024		
6.000-6.200	25.1	0.121 ± 0.100	0.026 ± 0.020		

Note. (1) Each redshift bin selected to calculate the pathlength density. (2) Average pathlength-weighted completeness over 31 sightlines. (3) Number of absorbers per unit redshift dz. (4) Number of absorbers per comoving absorption distance dX.

3.2. dN/dz and dN/dX

We calculate the incompleteness-corrected line-of-sight density of strong Mg II absorbers at different redshift bins. The results at four redshift bins between 2.2 and 6.0 are shown in Figure 8 and Table 3. The relation between dN/dz and redshift can be expressed as,

$$\frac{dN}{dz} = N_0 \times (1+z)^{\beta},\tag{10}$$

where N_0 is the normalization and β is the slope. We apply the maximum likelihood estimation method to the relation and find that N_0 and β are 1.882 ± 3.252 and -0.952 ± 1.108 , respectively.

Previous studies (e.g., M12 and C17) have found that the dN/dz of strong Mg II absorbers generally decreases with increasing redshift at 2 < z < 6. In particular, the dN/dz or dN/dX at z > 4.5 drops rapidly (see Figure 8). Codoreanu et al. (2017) studied Mg II systems using four quasars from VLT-Xshooter and found that the dN/dz is relatively flat at $2 < z \le 4$. This is

likely due to the larger uncertainties from their small sample, as they have pointed out in the paper. As shown in Figure 8, our results are consistent with the previous results within errors. The trend at 2 < z < 4 is not clear due to the large errors, but the density decreases significantly at z > 4.5.

3.3. Kinematics and Saturation

The evolution of Mg II incidence has implications for the origin of Mg II absorbers. One possible scenario is that superwinds give rise to strong Mg II absorbers in starburst galaxies (Bond et al. 2001; Heckman 2001; Bouché et al. 2006). Superwinds are gas bubbles generated by starbursts. They escape from gravitational wells and then blow into galaxy halos. Low-ions such as Mg II and Na I reside in the shells of these superwinds. Another possible scenario is that strong Mg II systems would reside in a galaxy groups environment. For example, Gauthier (2013) find their ultra-strong Mg II absorber ($W_r(\lambda 2796) = 4.2 \text{ Å}$) at z = 0.5624 is associated with five galaxies within 60 kpc.

To further investigate the possible scenarios for the origin of our strong Mg II systems, we compare the velocity widths of our Mg II systems with those at similar and lower redshift. We compare with three samples in the literature: a blindly searched Mg II sample from SDSS DR12 (Zhu & Ménard 2013) at 0.4 < z < 2.3, Mg II systems associated with a DLA sample from the XQ-100 survey at 2 < z < 4 (Berg et al. 2017), and Mg II systems traced by a neutral atomic carbon (C I) sample at 1.5 < z < 2.7 (Zou et al. 2018). The comparison is plotted in Figure 9.

We found that the velocity widths of our Mg II absorbers are larger than those associated with DLAs with similar equivalent widths at 2 < z < 4, this feature is also seen in C17 strong Mg II systems. In the C17 sample of 287 absorbers, 104 of which have $W_r(\lambda 2796) > 1$ Å, and 58 out of 104 have $\Delta v > 300 \, \mathrm{km \, s^{-1}}$. Note that the Δv given in C17 is defined as the

Quasar	z_{abs}	Targets NO.	R.A.	Decl.	F105W (mag)	M (mag)	D (kpc)	g (mag)	i (mag)	r (mag)	z (mag)
J0002+2550	3.059	1	00:02:39.24	+25:50:36.7	24.74 ± 0.08	-19.15 ± 0.08	20.2	>25.78			
J0050+3445	3.435	1	00:50:06.99	+34:45:22.8	24.83 ± 0.08	-19.20 ± 0.08	29.7	25.44 ± 0.10	25.64 ± 0.11		
		2	00:50:06.71	+34:45:18.5	23.96 ± 0.04	-20.07 ± 0.04	30.8	25.43 ± 0.10	24.89 ± 0.13		
J0842+1218	5.050	1	08:42:29.55	+12:18:52.5	24.72 ± 0.08	-19.72 ± 0.08	17.1	>25.64			
	2.540	1			24.72 ± 0.08	-18.94 ± 0.08	17.1				
	2.392	1			24.72 ± 0.08	-18.87 ± 0.08	21.9				
J1207+0630	3.808	1	12:07:37.61	+06:30:11.3	24.83 ± 0.12	-19.31 ± 0.12	21.5	>25.62			
	3.808	2	12:07:37.55	+06:30:13.9	25.10 ± 0.16	-19.04 ± 0.12	30.1				
J1250+3130	4.201	1	12:50:51.93	+31:30:23.6	25.49 ± 0.16	-18.76 ± 0.16	11.4	>25.61			
	3.860	1			25.49 ± 0.16	-18.66 ± 0.16	11.8				
	2.292	1			25.49 ± 0.16	-18.04 ± 0.16	13.7				
J1335+3533	4.530	1	13:35:50.68	+35:33:11.5	23.69 ± 0.04	-20.63 ± 0.04	30.7				
J2310+1855	4.244	1	23:10:38.73	+18:55:17.2	24.26 ± 0.05	-20.00 ± 0.05	22.6			25.55 ± 0.14	24.34 ± 0.25
	4.244	2	23:10:38.95	+18:55:22.6	25.10 ± 0.11	-19.15 ± 0.11	21.4			26.18 ± 0.25	

9

Note. The selection criteria is $\Delta v > 300 \text{ km s}^{-1}$ or $W_r(\lambda 2796) > 1.5 \text{ Å}$. The 1 or 2 labels in the third column are galaxy candidates numbers in Figures 8 and 9. Two detection limit in g band for J0002+2550, J0842 +1218, J1207+0630, and J1250+3130 are measured from public DECaLs imaging data. The g; r bands magnitudes for J0500+3445 and r; z bands magnitudes for J2310+1855 are measured from CFHT–MegaPrime.

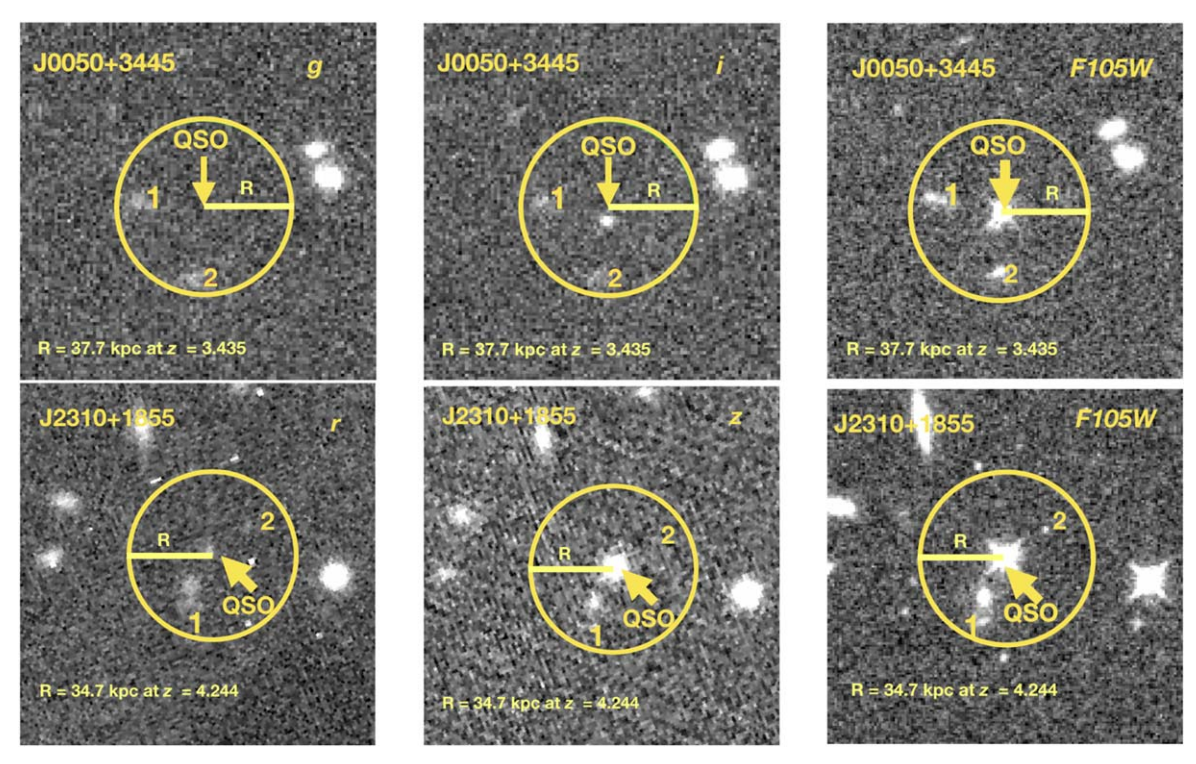


Figure 10. Image cutouts of J0050+3445 and J2310+1855. The g, i band images of J0500+3445 and r, z band images of J2310+1855 are from CFHT-MegaPrime. The F105W-band images are from HST. Image size is $20'' \times 20''$, the yellow circle is in a 5'' radius. The candidate absorber galaxies are denoted as 1 and 2.

total velocity interval under the continuum. Even if only 90% of their intervals are considered, half of the strong absorbers still have $\Delta v > 300 \, \mathrm{km \, s^{-1}}$. In the DLA-tracing Mg II sample, 18 out of 29 Mg II absorbers have $W_r > 1 \text{ Å}$ but only one has velocity width greater than $300 \, \mathrm{km \, s^{-1}}$. Moreover, large velocity widths for Mg II absorbers are also seen in the C Itracing Mg II absorbers at 1.5 < z < 2.7. The velocity widths were measured by the same method described in Section 2.2. In the 17 systems of C I-tracing Mg II absorbers, 15 have W_r > 1 Å and 13 out of 15 (87%) have $\Delta v > 300 \text{ km s}^{-1}$. C I has been shown to effectively trace molecular and cold gas at $z \sim 2$, and thus star formation activities. As discussed in Zou et al. (2018), the C I systems can be highly disturbed by superwinds or the interactions between several galaxies. Therefore, large velocity widths of our Mg II absorber suggest that our systems are potentially strongly affected by the galactic superwinds and/or the interaction within galaxy groups.

The two dashed lines in panel (b) are for $W_r(\lambda 2803)/W_r(\lambda 2796)=1$ and 0.5, respectively. The ratio greater than one implies that Mg II doublets are strongly saturated. In our sample, about 42% of the absorbers have this line ratio greater than 0.8. This fraction is $\sim 55\%$ in the 0.4 < z < 2.3 SDSS sample. Our Mg II systems are slightly less saturated than the absorbers at z < 2.3.

Another piece of possible supportive evidence is the equivalent width ratio of Fe II and Mg II lines $(W_r(\lambda 2600)/W_r(\lambda 2796))$. We compare our sample with the DLA-tracing Mg II sample at 2 < z < 4 and a sample from Rodríguez Hidalgo et al. (2012) at low redshift. Rodríguez Hidalgo et al. (2012) analyzed 87 Mg II system with $W_r(\lambda 2796) > 0.3$ Å at 0.2 < z < 2.5. They found that strong systems $(W_r(\lambda 2796) > 1$ Å) do not have small $W_r(\lambda 2600)/W_r(\lambda 2796)$ ratios in their sample. In panel (c) of Figure 9, our sample covers a wide range of the $W_r(\lambda 2600)/W_r(\lambda 2796)$ ratios. In particular, four systems among

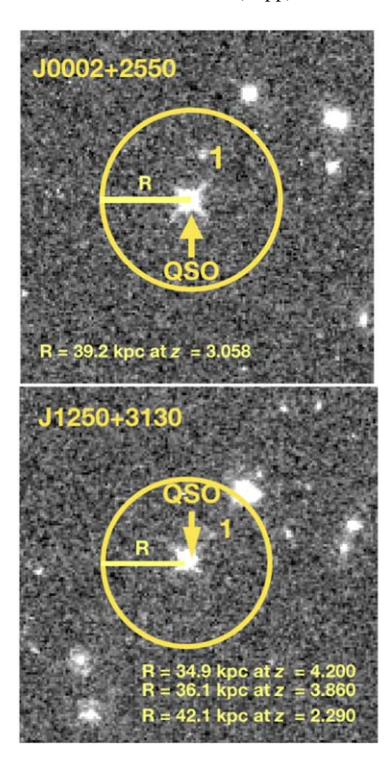
the strongest Mg II absorbers have smaller ratios $(W_r (\lambda 2600)/W_r (\lambda 2796) < 0.5)$ than most of the other systems in the sample. The small $W_r(\lambda 2600)/W_r(\lambda 2796)$ values can be due to many reasons, e.g., kinematics evolution, dust depletion, and intrinsic [Mg/Fe] abundance in the gas phase. We here propose that the kinematic evolution of the profiles of the very strong absorbers is a possible reason. Which means, at high redshift, the number of unresolved subcomponents associated with strong Mg II absorbers may grow.

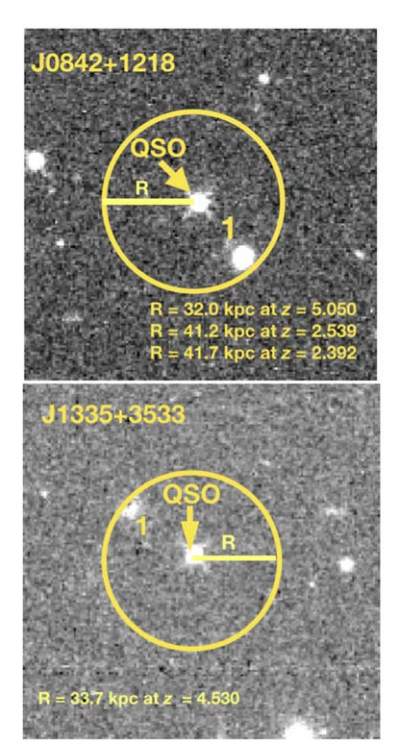
4. Discussion

Our strong Mg II systems exhibit large rest-frame velocity widths and potentially less saturation, the Mg II gas is potentially strongly affected by galactic superwinds or the interaction within galaxy groups. Previous studies suggest that both star-forming and passive galaxies may host Mg II absorbers. Star-forming galaxies tend to host stronger absorbers. Zibetti et al. (2007) studied 2,800 Mg II systems having $W_r(\lambda 2796) > 0.8$ Å at 0.37 < z < 1 and associated galaxies within 20-100 kpc. They tentatively conclude that $W_r(\lambda 2796) < 1.1 \,\text{Å}$ systems are associated with passive galaxies, while $W_r(\lambda 2796) > 1$ Å systems tend to be associated with star-forming galaxies. Lan et al. (2014) selected 2,000 galaxy-Mg II absorber pairs at z < 0.5 and found that, within 50 kpc, strong absorbers tend to be associated with star-forming galaxies. In this section, we will investigate the gas properties of the Mg II clouds, including gas cross-section, absorbing halo size, and the galaxy impact parameter.

4.1. HST Images

We have a small sample of HST snapshot images observed in the WFC3/IR F105W band (Program ID: 12184, PI: X. Fan). The images cover seven of our quasars with strong absorbers with $W_r(\lambda 2796) > 1.5 \,\text{Å}$ or $\Delta v > 300 \, \text{km s}^{-1}$,





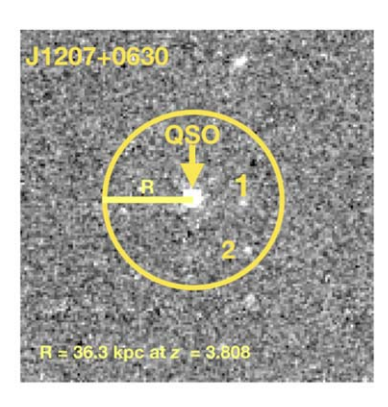


Figure 11. HST F105W-band image cutouts for J0002+2550, J0842+1218, J1207+0630, J1250+3130, J1335+3533, J1429+5447, and J1602+4228. Each figure size is $20'' \times 20''$, the yellow circle is in a 5'' radius. The possible nearby galaxy are denoted as 1 or 2.

namely J0002+2550, J0050+3445, J0842+1218, J1207+0630, J1250+3130, J1335+3533, J2310+1855. The median redshift of the absorbers is 3.982. For each quasar, there is at least one candidate galaxy with $\geqslant 7\sigma$ detection ($\leqslant 25.5$ mag) within a 5" circular radius in the HST image (see Table 4 and Figures 10 and 11). The photometry is performed using SExtractor (Bertin & Arnouts 1996). All these galaxies are fainter than 24 mag in F105W, which is fainter than L^* galaxies at $z\sim 4$ ($m^*=23.31\pm0.08$) (Bouwens et al. 2015). The median magnitude in F105W for our sample is 24.78.

The rest-frame band of F105W at the median redshift of Mg II (z=3.743) is U band. The Lyman-Break Galaxies UV-continuum slope γ ($f_{\lambda}=\lambda^{\gamma}$) measured by Bouwens et al. (2012) at $z\sim4$ is around -2, therefore we have $u-b\sim0$. If the galaxy is a passive galaxy, it is unable to be detected with present images. We then obtained $L_B/L_B^*=0.25$, where L_B and L_B^* are the B band luminosity of our galaxy candidates and L^* galaxies, respectively. The result is consistent with the estimates of the Mg II associated galaxy luminosity in M12.

Because we only have a single photometric band measurement, we do not know their redshifts or whether they are associated with the detected absorption systems. We search the archival images of the Dark Energy Camera Legacy Survey (DECaLS; Dey et al. 2019) and find that four quasar fields are covered by DECaLS (J0002+2550, J0842+1218, J1207+0630, J1250+3130). None of the above galaxies are detected in the grz bands. The 2σ detection limit in the g band (the deepest band) is roughly 25.5 mag (see also Table 4). The red g-F105W color implies that these galaxies are likely at high redshift. We further estimate the surface density of z > 2.5 galaxies brighter than 25.5 mag in a few HST fields (Bouwens et al. 2015) and find that the expected number of random galaxies in a 5" circular area is about 0.1. This is significantly

lower than our density of >1, suggesting that the galaxies detected in F105W above are likely associated with the strong absorbers. We can see that within 50 kpc of each absorber, we detected maximum two galaxy candidates. If multiple galaxies are associated with strong Mg II systems at high redshift, we need higher resolution spectra to disentangle the absorbing gas kinematic structure and deeper images to search for galaxy candidates nearby.

4.2. Gas Halo Size and Galaxy Impact Parameter

We have limited our search of galaxy candidates within a 5'' (42.36 kpc at z=2.2) radius, and we detected at least one candidate for each absorber within an impact parameter D=50 kpc. This median distance of 23.31 kpc is smaller than the median distance, $\langle D \rangle = 48.7$ kpc found in the local universe (Schulze et al. 2012; Nielsen et al. 2013a, 2013b, 2018), suggesting that strong Mg II absorbers likely have smaller impact parameters at higher redshift. We can also calculate the absorbing halo gas size from the measured dN/dX and L_B/L_B^* using the relation from Kacprzak et al. (2008). The comoving line density (dN/dz) can be expressed as the product of the absorber physical cross-section σ and volume comoving number density n(z),

$$\frac{dN}{dz} = \frac{c}{H_0} \sigma n(z) \frac{dX}{dz},\tag{11}$$

where c/H_0 is the constant of proportionality and

$$\frac{dX}{dz} = \frac{(1+z)^2}{\sqrt{\Omega_m (1+z)^3 + \Omega_\Lambda}}.$$
 (12)

The gas cross-section is expressed as $\sigma = \pi R_x^2$, where R_x is the absorbing gas halo size. The volume number density n(z) can

be expressed as a function of associated galaxy luminosity:

$$n(z) = \Phi^* \times \Gamma(x, y), \tag{13}$$

where Φ^* is the number density of L^* galaxies in the galaxy luminosity function. $\Gamma(x, y)$ is an incomplete Gamma function with $x = 2\beta - \alpha + 1$, where α is the faint-end slope of Schechter function and β is the factor of a relation between R_x and associated galaxy luminosity (Steidel et al. 1995): $R_x = R_* \times (L/L^*)^\beta$. y is the ratio of the detected galaxy minimum luminosity to L^* . Therefore R_x is:

$$R_{x} = \sqrt{\frac{dN/dX}{\pi \Phi^{*} \Gamma(x, y)}}.$$
 (14)

We take $\alpha=-1.64\pm0.04$ from Bouwens et al. (2015), $\beta=0.35$, our measured $y=L_B/L_B^*=0.25$ and dN/dz at $\langle z\rangle=3.5$, $\Phi_B^*=1.97^{+0.34}_{-0.28}\times10^{-3}$ Mpc⁻³ (Bouwens et al. 2015) to calculate the R_x . The β value is from Chen et al. (2010), which analyzed 47 Mg II associated galaxies at z<0.5 and with $0.1< W_r(\lambda 2796)<2.34$ Å. We assume the slope does not change at higher redshift. The R_x is then estimated as follows:

$$R_x(\text{kpc}) = \begin{cases} 37, & \beta = 0.35, \ y = 0.05; \\ 8, & \beta = 0.35, \ y = 0.25. \end{cases}$$
 (15)

With our measured $L_B/L_B^*=0.25$, R_x is smaller than the possible D. This is based on the assumption that the covering fraction f_c of the gas is unity. The covering fraction of the absorbing gas is defined as the ratio of absorbers associated galaxies and all galaxies at the same redshift bin. Lan (2020) found that the covering fraction of strong Mg II systems evolves with redshift at 0.4 < z < 1.3, similarly to the evolution of SFR of galaxies. In the study of Chen et al. (2010), the Mg II-absorbing halo gas covering fraction is 70% for $W_r(\lambda 2796) > 0.3$ Å. Nielsen et al. (2018) studied 74 galaxies at 0.113 < z < 0.888 with $\langle W_r(\lambda 2796) \rangle = 0.65$ Å, and found $f_c = 0.68$ for isolated galaxies. Since we have 1–2 galaxy candidates within 5" of the absorber, we adopt the $f_c = 0.68$. The covering fraction corrected size R_* is 9.23 kpc $(R_x^2 = f_c R_*^2)$, which is still smaller than the $\langle D \rangle = 23.31$ kpc.

In summary, we searched for associated galaxies around our strong Mg II absorbers at z=3–5.1 within 50 kpc and found 1–2 candidates for each absorber. The galaxy candidates are brighter than 25.5 mag and have a median magnitude of 24.78 in F105W band. These candidates have a median impact parameter $\langle D \rangle = 23.31$ kpc, which is smaller than that at z < 1. If we assume that the R_x –L slope and f_c for strong Mg II absorbers at z=3–5.1 are similar to that at z<1, with a fixed associated galaxy luminosity $L=0.25L^*$ and a covering fraction of $f_c=0.68$, the f_c -corrected absorbing halo gas R_* is smaller than the $\langle D \rangle$. In other words, within 50 kpc, high redshift strong Mg II absorbers tend to have a more disturbed environment but smaller halo size than that at z<1.

4.3. Individual Systems

In this subsection, we present a few individual systems with peculiar absorption features or having images in other bands. J0050+3445. We detected a Mg II absorber at z=3.435

with $W_r(\lambda 2796) = 3.44 \pm 0.88 \,\text{Å}$. There are two galaxy

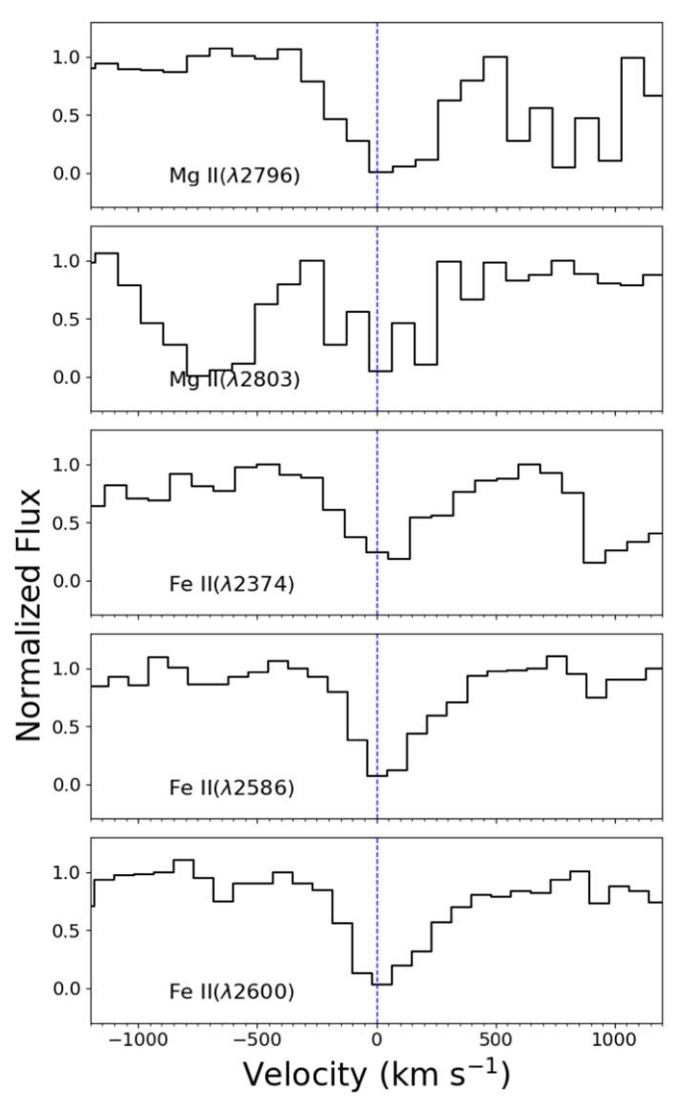


Figure 12. Velocity profile of J1148+0702 at z=4.369. This system has Mg II absorption $(W_r(\lambda 2796)=4.23\pm0.52\text{ Å})$ and the strongest Fe II absorption $(W_r(\lambda 2600)=3.61\pm0.54\text{ Å})$ in the whole sample. However, there is no image data for this quasar in HST, CFHT, DECaLS, and Pan-STARRS archives.

candidates within 5" from the quasar, labeled as 1 and 2 in Figure 10. We measure the g and r band magnitudes of the two objects using archived Canada–France–Hawaii Telescope (CFHT) MegaPrime images. The magnitudes of galaxy 1 are $g=25.44\pm0.10$ and $i=25.64\pm0.11$. The magnitudes of galaxy 2 are $g=25.43\pm0.10$ and $i=24.89\pm0.13$. The Ly α emission line at z=3.435 is redshifted to 5391 Å (g band), so galaxy 2 with g-i=0.54 is more likely to be the absorber.

J2310+1855. We detected strong Mg II and Fe II at z=4.244. In Figure 10 there are two galaxies within 5" (25 kpc) from the quasar. The magnitudes of galaxy 1 are $r=25.55\pm0.14$, $z=24.34\pm0.25$, and $F105W=24.26\pm0.05$. The magnitudes of galaxy 2 are $r=26.18\pm0.25$ and $F105W=25.10\pm0.11$. It is not detected in z. Based on their colors, galaxy 1 is more likely to be the absorber host at z=4.244. In addition, there is a bright object next to galaxy 1. But its $m_z=22.15$ is much brighter than L^* at $z\sim4$, so we did not consider it.

J1148+0702. We detected Mg II and Fe II at z=4.369 and z=3.495, the latter one has extremely large velocity spread for a Mg II doublet. This one at z=4.369 has a very strong Mg II $(W_r(\lambda 2796)>4 \,\text{Å})$ absorber with the strongest Fe II $(W_r(\lambda 2600)=4.45\pm0.82 \,\text{Å})$ absorption in our sample. Both Mg II and Fe II lines are strongly saturated. As discussed in Joshi et al. (2017), strong Mg II and Fe II in the same system may indicate star formation nearby. We do not have HST images for this quasar. The Mg II and Fe II absorption profiles are presented in Figure 12.

5. Conclusion

We have analyzed the near-IR spectra of 31 luminous quasars at z > 5.7, selected from a sample of 50 quasars observed by Gemini GNIRS. We identified 32 Mg II and Fe II absorbers with Mg II $W_r(2796) > 1.0$ Å at 2.2 < z < 6.0. We calculated the line density dN/dz and comoving line density dN/dX of the strong Mg II absorbers and found that they decrease toward higher redshift at z > 3. This can be described by the relation $dN/dz = (1.882 \pm 3.252) \times (1+z)^{-0.952 \pm 1.108}$. The trend is consistent with previous results, and follows the evolution of the cosmic SFR, implying the correlation between strong Mg II absorbers with the star formation of galaxies at high redshift.

We found that 15/32 of our Mg II systems have large velocity widths with $\Delta v > 300 \, \mathrm{km \, s^{-1}}$, which is much larger than those detected in DLA systems with similar equivalent widths at 2 < z < 4 and Mg II systems at z < 2. Such large velocity widths are also seen in a sample of neutral-carbon selected Mg II systems at 1.5 < z < 2.7. This potentially implies that strong Mg II systems at high redshift are influenced by galactic superwinds and/or interaction within galaxy groups. Also, our Mg II systems exhibit slightly less saturation in terms of the equivalent width ratio of Fe II and Mg II lines $(W_r(\lambda 2600)/W_r(\lambda 2796))$. For DLA systems, $W_r(\lambda 2600)/W_r(\lambda 2796) \sim 0.5$. This ratio is roughly between 0.25 and 1.75 in our sample. Our Mg II absorbers are possibly less saturated than DLA-Mg II at 2 < z < 4 and those at z < 2.3 with similar equivalent widths. This is potentially caused by the interaction of more subcomponents of our strong Mg II systems.

We have used several HST images (together with archival DECaLS and CFHT images) to identify potential absorber galaxies within 50 kpc from quasars. For Mg II systems that have $\Delta \nu > 300 \, \mathrm{km \, s^{-1}}$ or $W_r(\lambda 2796) > 1.5 \, \mathrm{\mathring{A}}$, there are 1–2 galaxy candidates within the 5" radius. The median F105W-band magnitudes is 24.83 mag, which is fainter than the L^* galaxy luminosity at $z \sim 4$. If the Mg II-absorbing halo gas and associated galaxy luminosity relation at z = 3–5 is similar to that at z < 1, the Mg II absorbing gas size R_x is smaller than D.

We thank the very constructive comments and suggestions from the anonymous referee. We thank Patrick Petitjean for useful comments and Robert A. Simcoe for discussion on FIRE data. We acknowledge support from the National Science Foundation of China (11533001, 11721303, 11890693, 11991052), the National Key R&D Program of China (2016YFA0400702, 2016YFA0400703), and the Chinese Academy of Sciences (CAS) through a China-Chile Joint Research Fund #1503 administered by the CAS South America Center for Astronomy in Santiago, Chile. Y.S.

acknowledges support from an Alfred P. Sloan Research Fellowship and National Science Foundation grant No. AST-1715579. M.V. gratefully acknowledges financial support from the Independent Research Fund Denmark via grant No. DFF 8021-00130. We acknowledge the public data from the Dark Energy Camera Legacy Survey (DECaLS), the Beijing-Arizona Sky Survey (BASS), and the Mayall *z*-band Legacy Survey (MzLS). We thank observations obtained with MegaPrime/MegaCam, a joint project of CFHT and CEA/DAPNIA, at the Canada–France–Hawaii Telescope (CFHT), which is operated by the National Research Council (NRC) of Canada, the Institut National des Science de l'Univers of the Centre National de la Recherche Scientifique (CNRS) of France, and the University of Hawaii.

Facility: Gemini(GNIRS).

ORCID iDs

```
Siwei Zou https://orcid.org/0000-0002-3983-6484
Linhua Jiang https://orcid.org/0000-0003-4176-6486
Yue Shen https://orcid.org/0000-0003-1659-7035
Jin Wu https://orcid.org/0000-0001-5364-8941
Eduardo Bañados https://orcid.org/0000-0002-2931-7824
Xiaohui Fan https://orcid.org/0000-0003-3310-0131
Luis C. Ho https://orcid.org/0000-0001-6947-5846
Dominik A. Riechers https://orcid.org/0000-0001-
9585-1462
Bram Venemans https://orcid.org/0000-0001-9024-8322
Marianne Vestergaard https://orcid.org/0000-0001-
9191-9837
Fabian Walter https://orcid.org/0000-0003-4793-7880
Feige Wang https://orcid.org/0000-0002-7633-431X
Chris J. Willott https://orcid.org/0000-0002-4201-7367
Ravi Joshi https://orcid.org/0000-0002-5535-4186
Xue-Bing Wu https://orcid.org/0000-0002-7350-6913
Jinyi Yang https://orcid.org/0000-0001-5287-4242
```

References

```
Berg, T. A. M., Ellison, S. L., Prochaska, J. X., et al. 2017, MNRAS, 464, L56
Bergeron, J., & Boissé, P. 1991, A&A, 243, 344
Bertin, E., & Arnouts, S. 1996, A&AS, 117, 393
Bond, N. A., Churchill, C. W., Charlton, J. C., & Vogt, S. S. 2001, ApJ,
  562, 641
Bouché, N., Murphy, M. T., Kacprzak, G. G., et al. 2013, Sci, 341, 50
Bouché, N., Murphy, M. T., Péroux, C., Csabai, I., & Wild, V. 2006, MNRAS,
  371, 495
Bouwens, R. J., Illingworth, G. D., Oesch, P. A., et al. 2012, ApJ, 754, 83
Bouwens, R. J., Illingworth, G. D., Oesch, P. A., et al. 2015, ApJ, 803, 34
Chen, H.-W., Helsby, J. E., Gauthier, J.-R., et al. 2010, ApJ, 714, 1521
Chen, S.-F. S., Simcoe, R. A., Torrey, P., et al. 2017, ApJ, 850, 188
Codoreanu, A., Ryan-Weber, E. V., Crighton, N. H. M., et al. 2017, MNRAS,
  472, 1023
Dey, A., Schlegel, D. J., Lang, D., et al. 2019, AJ, 157, 168
Gauthier, J.-R. 2013, MNRAS, 432, 1444
Heckman, T. M. 2001, in ASP Conf. Ser. 240, Galactic Superwinds at Low and
  High Redshift, ed. J. E. Hibbard, M. Rupen, & J. H. vanGorkom (San
  Francisco, CA: ASP), 345
Jiang, L., McGreer, I. D., Fan, X., et al. 2016, ApJ, 833, 222
Joshi, R., Srianand, R., Noterdaeme, P., & Petitjean, P. 2017, MNRAS,
  465, 701
Kacprzak, G. G., Churchill, C. W., Evans, J. L., Murphy, M. T., &
  Steidel, C. C. 2011, MNRAS, 416, 3118
Kacprzak, G. G., Churchill, C. W., Steidel, C. C., & Murphy, M. T. 2008, AJ,
   135, 922
Krogager, J.-K. 2018, arXiv:1803.01187
Lan, T.-W. 2020, ApJ, 897, 97
Lan, T.-W., Ménard, B., & Zhu, G. 2014, ApJ, 795, 31
```

Lanzetta, K. M., Turnshek, D. A., & Wolfe, A. M. 1987, ApJ, 322, 739

```
Lovegrove, E., & Simcoe, R. A. 2011, ApJ, 740, 30
Martin, C. L., & Bouché, N. 2009, ApJ, 703, 1394
Mason, R. E., Rodríguez-Ardila, A., Martins, L., et al. 2015, ApJS, 217, 13
Matejek, M. S., & Simcoe, R. A. 2012, ApJ, 761, 112
Ménard, B., & Fukugita, M. 2012, ApJ, 754, 116
Ménard, B., Wild, V., Nestor, D., et al. 2011, MNRAS, 417, 801
Nestor, D. B., Turnshek, D. A., & Rao, S. M. 2005, ApJ, 628, 637
Nestor, D. B., Turnshek, D. A., Rao, S. M., & Quider, A. M. 2007, ApJ,
Nielsen, N. M., Churchill, C. W., & Kacprzak, G. G. 2013a, ApJ, 776, 115
Nielsen, N. M., Churchill, C. W., Kacprzak, G. G., & Murphy, M. T. 2013b,
   ApJ, 776, 114
Nielsen, N. M., Kacprzak, G. G., Pointon, S. K., Churchill, C. W., &
   Murphy, M. T. 2018, ApJ, 869, 153
Noterdaeme, P., Petitjean, P., Ledoux, C., et al. 2010, A&A, 523, A80
Prochaska, J. X., Worseck, G., & O'Meara, J. M. 2009, ApJL, 705, L113
Prochter, G. E., Prochaska, J. X., & Burles, S. M. 2006, ApJ, 639, 766
Quider, A. M., Nestor, D. B., Turnshek, D. A., et al. 2011, AJ, 141, 137
Rao, S. M., Turnshek, D. A., & Nestor, D. B. 2006, ApJ, 636, 610
```

```
Rodríguez Hidalgo, P., Wessels, K., Charlton, J. C., et al. 2012, MNRAS,
  427, 1801
Rubin, K. H. R., Prochaska, J. X., Koo, D. C., & Phillips, A. C. 2012, ApJL,
  747, L26
Schroetter, I., Bouché, N., Wendt, M., et al. 2016, ApJ, 833, 39
Schroetter, I., Bouché, N. F., Zabl, J., et al. 2019, MNRAS, 490, 4368
Schulze, S., Fynbo, J. P. U., Milvang-Jensen, B., et al. 2012, A&A, 546, A20
Shen, Y., Wu, J., Jiang, L., et al. 2019, ApJ, 873, 35
Steidel, C. C., Bowen, D. V., Blades, J. C., & Dickinson, M. 1995, ApJL,
  440, L45
Steidel, C. C., Dickinson, M., Meyer, D. M., Adelberger, K. L., &
  Sembach, K. R. 1997, ApJ, 480, 568
Steidel, C. C., Kollmeier, J. A., Shapley, A. E., et al. 2002, ApJ, 570, 526
Tumlinson, J., Peeples, M. S., & Werk, J. K. 2017, ARA&A, 55, 389
Vollmann, K., & Eversberg, T. 2006, AN, 327, 862
Zabl, J., Bouché, N. F., Schroetter, I., et al. 2019, MNRAS, 485, 1961
Zhu, G., & Ménard, B. 2013, ApJ, 770, 130
```

Zibetti, S., Ménard, B., Nestor, D. B., et al. 2007, ApJ, 658, 161

Zou, S., Petitjean, P., Noterdaeme, P., et al. 2018, A&A, 616, A158